Vibrational Spectroscopy of Intermediates and C-H Activation Products of Sequential Zr^+ Reactions with CH_4

Justine Kozubal, Tristan Heck, and Ricardo B. Metz*

Department of Chemistry, University of Massachusetts, Amherst Amherst, Massachusetts 01003, United States

E-mail: rbmetz@chem.umass.edu

Phone: +1-413-545-6089. Fax: +1-413-545-4490

Abstract

Vibrational spectra of the entrance channel complexes $Zr^+(CH_4)_n(Ar)$ (n=1-2), $Zr^+(CH_4)_n$ (n=3-4), and the reaction products $ZrC_3H_{10}^+$, $ZrC_4H_{13}^+$, $ZrC_4H_{14}^+$, and $ZrC_4H_{15}^+$ in the C-H stretching region (2550-3100 cm⁻¹) are obtained using photofragment spectroscopy. The experimental spectra and simulations based on calculations at the B3LYP/aug-cc-pVTZ level of theory work together to identify the structures of the ions. The n=1-3 entrance channel complexes show peaks around 2800 and 3000 cm⁻¹ which indicates methane η^3 hydrogen coordination, while the n=4 complex has two peaks around 2800 cm⁻¹ indicative of methane η^2 hydrogen coordination. Observation of the low-frequency C-H stretch of an agostic carbene group, as well as the high-frequency H-H stretch, also confirms production of $(H_2)ZrCH_2^+(CH_4)_{n-1}$ (n=1-2) exit channel complexes. The observed C-H activation products formally correspond to loss of H_2 from $Zr^+(CH_4)_3$ and loss of H, H_2 , and H_2 + H from $Zr^+(CH_4)_4$. Comparison

of experiment and simulations indicate the activation products are $\operatorname{Zr}(\operatorname{CH}_3)_2^+(\operatorname{CH}_4)$, $\operatorname{Zr}(\operatorname{CH}_3)_3^+(\operatorname{CH}_4)$, $\operatorname{Zr}(\operatorname{CH}_3)_2^+(\operatorname{CH}_4)_2$, and $\operatorname{HZrCH}_2^+(\operatorname{CH}_4)_3$ and/or $\operatorname{ZrCH}_3^+(\operatorname{CH}_4)_3$.

1 Introduction

The direct conversion of methane to a more industrially useful chemical has been a long-standing goal of catalysis, as it would convert an abundant, inexpensive feedstock into a liquid fuel or precursor for higher value chemicals. ¹⁻³ In addition, the activation of the C–H bond in the simplest stable hydrocarbon is of fundamental interest. Thus, when gasphase studies showed that the 5d transition-metal cations M^+ =Ta $^+$, W^+ , Os $^+$, Ir $^+$, and Pt $^+$ efficiently activate methane at room temperature, ⁴⁻⁸ forming MCH $_2^+$ + H $_2$, they inspired many investigations of these reactions. ⁹⁻¹³ Initially, the reaction of a transition metal and methane form an M^+ (CH $_4$) entrance channel complex (Reaction 1). ⁴ The metal can then insert into a C–H bond to form the [H–M–CH $_3$] $^+$ and [H–M(H)–CH $_2$] $^+$ intermediates, followed by the MCH $_2^+$ (H $_2$) exit channel complex, which then releases H $_2$ and forms the MCH $_2^+$ product. For the 5d M $^+$, sequential reactions with methane form ions as large as [MC $_8$ H $_{16}$] $^+$. ⁷

$$M^{+} + CH_{4} \rightarrow M^{+}(CH_{4}) \rightarrow [H-M-CH_{3}]^{+} \rightarrow [(H)_{2}MCH_{2}]^{+} \rightarrow (H_{2})MCH_{2}^{+} \rightarrow MCH_{2}^{+} + H_{2}$$
(1)

Dehydrogenation of CH_4 is significantly endothermic for all first- and most second-row transition metal cations; however, reaction is observed at high collision energies and for electronically excited M^+ .¹⁴ Guided ion beam studies show that reaction 1 is endothermic by $29 \pm 9 \text{ kJ/mol}^{15}$ for Nb⁺. As a result, it dehydrogenates methane at only 0.4% of the collision rate.⁹

An early study by Ranasinghe $et~al.^{16}$ reported that reaction of Zr⁺ with methane forms $ZrCH_2^+$ at room temperature; this was confirmed by van Koppen et~al., who observed that the $ZrCH_2^+$ subsequently reacts with methane to form $ZrCH_2^+(CH_4)$ and $ZrCH_2^+(CH_4)_2.^{17}$

However, Shayesteh et~al. did not observe dehydrogenation in room temperature reactions of Zr⁺ with CH₄ in 0.35 Torr of helium. [ZrCH₄]⁺ and [ZrC₂H₈]⁺ were the only observed products, and they are formed much more efficiently than for any other 3d or 4d metal. The key to understanding these seemingly disparate results is provided by guided ion beam studies by Armentrout and Sievers of the reactions of Zr⁺ with methane ¹⁸ and larger hydrocarbons ¹⁹ as a function of collision energy. They find that the dehydrogenation of CH₄ by Zr⁺ is barely endothermic, by 13 ± 5 kJ/mol, and that there are no barriers in excess of the endothermicity. As a result, at low pressure, dehydrogenation is likely, but at higher pressures, collisions would lead to stabilization of one of the reaction intermediates, which would then be trapped, leading to the observation of [ZrCH₄]⁺, which could be a Zr⁺(CH₄) entrance channel complex or any of the other intermediates in reaction 1.

The ability of zirconium to activate methane extends to the condensed phase. Wolczanski and coworkers showed that in solution the zirconium-imido complex $(t-Bu_3 SiNH)_2 Zr=NSit-Bu_3$, formed by thermolysis of $(t-Bu_3 SiNH)_3 Zr(R)$, efficiently activates a C-H bond in methane to form $(t-Bu_3 SiNH)_3 Zr(CH_3)$. Metal-methyl complexes have often been used as pre-catalysts for olefin polymerization. Fontaine $et\ al$. synthesized zirconium trimethyl imino-enamido complexes, which are thermally robust and exhibit higher catalytic activities than the imino-amido analogues. 22,23 These complexes are useful catalysts for making high molecular weight ethene and 1-octene co-polymers. In addition, ligated trimethyl complexes of zirconium have been made using preparative chemistry, and they are useful precursors to zirconium methylidenes. 24

Spectroscopy, and especially vibrational spectroscopy, is a valuable complement to mass spectrometry-based experiments, as it can identify the structures of the reaction intermediates and products, by comparing them to the calculated spectra of candidate structures. $^{25-29}$ In $M^+(CH_4)_n$ entrance channel complexes, interaction with the metal weakens the proximate C–H bonds in the methane, reducing the corresponding C–H stretching frequencies, as shown in vibrational spectroscopy studies of $Li^+(CH_4)_{1-9}$, 30 $Al^+(CH_4)_{1-6}$, 31 and the late trans-

sition metals $Mn^+(CH_4)_{1-6}$, 32 $Fe^+(CH_4)_{1-4}$, 33 $Co^+(CH_4)_{1-4}$, 34 $Ni^+(CH_4)_{1-4}$, 34 $Cu^+(CH_4)_{1-6}$, 35 $Ag^+(CH_4)_{1-6}$, 35 and $Au^+(CH_4)_{3-8}$. 36 There have also been electronic spectroscopy studies of $Mg^+(CH_4)$, 37 $Ca^+(CH_4)$, 38 $V^+(CH_4)$, 39 and $Zn^+(CH_4)$. 40

Vibrational spectroscopy is especially useful in identifying the reaction products. The structures of $\mathrm{MCH_2}^+$ produced by dehydrogenation of methane by the 5d transition metal cations have been identified as an agostic carbene (Ta^+ , W^+), 41,42 a C_{2v} carbene (Pt^+ , Au^+), $^{43-45}$ a carbyne hydride (Os^+), 46 and a mixture of both (Ir^+). 47 Sequential reaction of M^+ with methane can produce a wide variety of potential dehydrogenation products, via many possible pathways. 48 Wheeler *et al.* used infrared multiple photon dissociation (IRMPD) to determine that $\mathrm{PtCH_2}^+$ formed by dehydrogenation of $\mathrm{CH_4}$ by Pt^+ then activates a $\mathrm{C-H}$ bond in $\mathrm{CH_4}$ to form $\mathrm{Pt}(\mathrm{CH_3})_2^+$. Subsequent $\mathrm{CH_4}$ molecules are not activated, forming $\mathrm{Pt}(\mathrm{CH_3})_2^+$ ($\mathrm{CH_4})_{\mathrm{n-2}}$ adducts for $\mathrm{n=2-4.4^{44}\ Ir^+}$ sequentially reacts with $\mathrm{CH_4}$ to produce several products. Addition of a second $\mathrm{CH_4}$ leads to single and double dehydrogenation, producing $\mathrm{HIrCH_2}(\mathrm{CH_3})^+$ and $\mathrm{Ir}(\mathrm{CH_2})_2^+$ in the singlet state and $\mathrm{Ir}(\mathrm{CH_3})_2^+$ in the triplet state, while addition of the third $\mathrm{CH_4}$ leads to isomerization and formation of $\mathrm{HIr}(\mathrm{CH_3})_3^+$. 47

In this study, we report vibrational spectra of $\operatorname{Zr}^+(\operatorname{CH}_4)_n(\operatorname{Ar})$ (n=1-2), $\operatorname{Zr}^+(\operatorname{CH}_4)_n$ (n=3-4), and four C-H activation products, $\operatorname{ZrC}_3\operatorname{H}_{10}^+$, $\operatorname{ZrC}_4\operatorname{H}_{13}^+$, $\operatorname{ZrC}_4\operatorname{H}_{14}^+$, and $\operatorname{ZrC}_4\operatorname{H}_{15}^+$, measured via photofragment spectroscopy. The experimental results are compared with simulations of possible isomers to determine the lowest energy isomer, geometry, and method of C-H activation. These fundamental studies will help to provide a deeper understanding of the reaction mechanisms involved in hydrocarbon bond activation in more complex systems and will aid in the design of catalysts to convert methane into readily transportable liquid fuels.

2 Experimental and Computational Methods

The molecules are produced in a laser ablation source on a home-built dual time-of-flight reflectron mass spectrometer, which is described in detail elsewhere. ⁴⁹ The $Zr^+(CH_4)_n(Ar)$ (n=1-2) and $Zr^+(CH_4)_n$ (n=3-4) complexes are produced by ablating a zirconium rod that is continuously translating and rotating using the second harmonic (532 nm) of a Nd:YAG laser operating at 6 mJ/pulse with a repetition rate of 20 Hz. The gas is introduced through a pulsed valve (General Valve, Series 9) and consists of 0.025-2% CH_4 in pure He and, for tagged complexes, 20-30% Ar in He, with backing pressures ranging from 40 to 80 psi. The C-H activation products are made using 5% CH_4 in pure He at 10 psi with higher laser power (9-15 mJ/pulse). A mass spectrum obtained under these conditions is shown in Figure S1. All vibrational spectra are of the ^{90}Zr isotope. The ions travel through a 11 mm long, 2.5 mm ID tube after laser ablation.

Ions then expand into vacuum and cool, creating a molecular beam with a rotational temperature of about 15 K.⁵⁰ The ion beam is skimmed, extracted into the time-of-flight mass spectrometer, accelerated, and re-referenced to ground potential. The ions are mass selected and dissociated at the turning point of the reflectron by a Nd:YAG-pumped OPO/OPA IR laser system (LaserVision), which produces about 7-9 mJ/pulse near 3000 cm⁻¹, with a line width of 1.8 cm⁻¹. The laser wavelength is calibrated using the absorption spectrum of methane.⁵¹

The parent and photofragment ions are re-accelerated in the second time-of-flight stage and hit a 40 mm dual microchannel plate detector. The ion masses are determined from their characteristic flight times. The ion signal is amplified and collected on a gated integrator and a LabView based program is used to record the data. The photodissociation spectrum is obtained by first normalizing the fragment signal to the parent signal, and then to laser power as a function of wavelength. The observed fragments correspond to loss of one or more intact CH_4 from $Zr^+(CH_4)_n$ (n=3-4) and the reaction products, and Ar from $Zr^+(CH_4)_n$ (Ar) (n=1-2).

A second, fast-flow reactor source, shown in detail in Figure S2, was used to reproduce spectra from the first setup. This source uses two pulsed valves, so that the $\rm Zr^+$ ions are produced and thermalized in one region, then react with methane which is introduced downstream. The primary valve contains pure helium at a backing pressure of 40 psi. The secondary valve sits 23 mm after the primary valve and contains a gas mixture of 5% $\rm CH_4$ in He at a backing pressure of 6 psi.

The fast-flow reactor source is used to take spectra of $Zr^+(CH_4)_3$, $Zr^+(CH_4)_4$, and $ZrC_3H_{10}^+$ to determine if the same molecules are being made via reactions of thermalized Zr^+ ions. The spectra produced with this setup match the spectra with the one-valve setup, indicating the same molecules are being produced with both sources; however, the ion signal is much lower with the fast-flow reactor source. All the spectra presented in this paper are taken with the one-valve setup except for $Zr^+(CH_4)_4$ which has less background with the fast-flow reactor source.

Calculations are carried out with the Gaussian09 program package.⁵² Optimized geometries of the ions are computed using the B3LYP density functional and the aug-cc-pVTZ basis set. We find that B3LYP is better at predicting the vibrational frequencies of $M^+(CH_4)_n$ systems than newer functionals such as M11L.⁵³ However, the M11L functional does a better job at predicting the spectra of the reaction products. All calculations are carried out with both functionals, with the M11L results shown in the SI. All reported energies include zero-point energy. Vibrational frequencies are scaled by 0.964 based on the ratio of the experimental and computed values of the symmetric and antisymmetric C-H stretching frequencies of CH_4 .

The accuracy of the B3LYP and M11L functionals in predicting thermodynamics for the reactions of interest can be assessed by comparing calculated and available experimental bond dissociation energies (BDEs), as shown in Table 1. For these reactions, M11L consistently predicts higher BDEs, by an average of 21 kJ/mol. However, neither functional is clearly better when compared to the measured values, with mean unsigned errors of 28.7 kJ/mol

(B3LYP) and 27.3 kJ/mol (M11L). As expected, both functionals more accurately predict C-H bond dissociation energies.

Table 1: Zr⁺-L and Methane Bond Dissociation Energies, in kJ/mol

Species	$B3LYP^a$	$M11L^a$	Experiment
Zr ⁺ -H	234.6	245.2	218 ± 8^{b}
Zr^+ - H_2	32.8	43.5	60.8 ± 1.0^{c}
Zr^+ - CH	528.6	548.1	568 ± 13^{d}
$\mathrm{Zr}^+\text{-}\mathrm{CH}_2$	419.1	459.3	445 ± 5^{d}
Zr^+ - CH_3	261.2	284.9	228 ± 10^{d}
$\mathrm{CH_{3} ext{-}H}$	425.1	432.5	432.46 ± 0.03^e
$\mathrm{CH_2} ext{-}\mathrm{H_2}$	450.3	449.6	457.62 ± 0.10^{e}

^aCalculations use the aug-cc-pVTZ basis set, are at zero Kelvin and include zero point energy ^bRef. ⁵⁴ ^cRef. ⁵⁵ ^dRef. ¹⁹ ^eRef. ⁵⁶

3 Results and Discussion

Photofragment spectroscopy is used to measure the vibrational spectra of the entrance channel complexes $Zr^+(CH_4)_n(Ar)$ (n=1-2) and $Zr^+(CH_4)_n$ (n=3-4), and the reaction products $ZrC_3H_{10}^+$, $ZrC_4H_{13}^+$, $ZrC_4H_{14}^+$, and $ZrC_4H_{15}^+$ in the C-H stretching region (2550-3100 cm⁻¹). The entrance channel complexes will be discussed in Section 3.1, followed by the methane activation products in Section 3.2.

$3.1 ext{ } ext{Zr}^+(CH_4)_n$

The spectra of the entrance channel complexes, shown in Figure 1, show peaks significantly red shifted from the symmetric (ν_1 =2917 cm⁻¹) and antisymmetric (ν_3 =3019 cm⁻¹) C–H stretches in bare CH₄. Although the symmetric stretch in bare CH₄ is not IR active, binding to the metal weakens and polarizes the proximate C–H bonds, leading to a substantial red shift in their stretching frequency and strong IR absorption. As a result, the symmetric stretch is more intense than the antisymmetric stretch. The peak at 2730 cm⁻¹ in smaller clusters shifts slightly to higher wavenumbers with increasing cluster size.

The n=1-3 clusters all have a peak near the antisymmetric stretch in bare CH_4 while this is absent for n=4. The spectra of $Zr^+(CH_4)(Ar)$ and $Zr^+(CH_4)_2(Ar)$ also have one small peak below 2600 cm⁻¹. The spectra, structures, and corresponding simulations of each entrance channel complex will be discussed in the following sections.

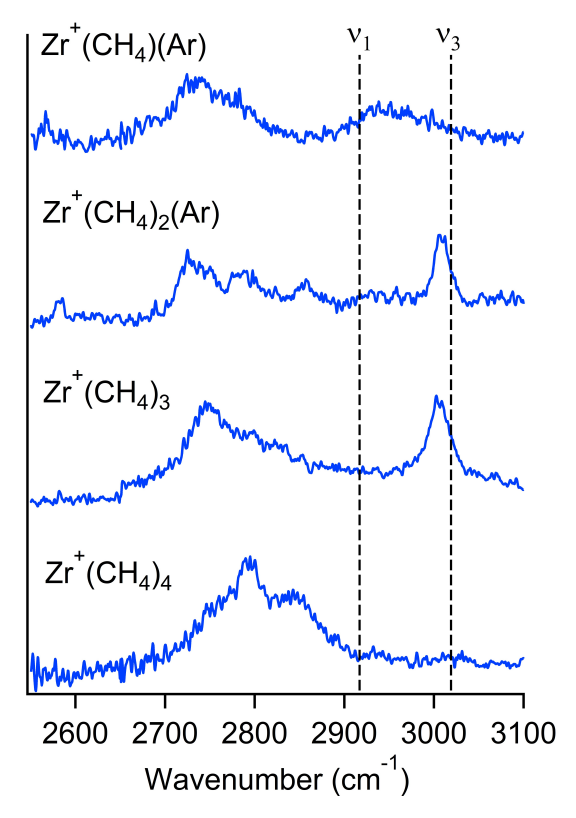


Figure 1: Vibrational spectra of $Zr^+(CH_4)_n(Ar)$, (n=1-2) and $Zr^+(CH_4)_n$, (n=3-4) in the C–H stretching region (2550-3100 cm⁻¹). The symmetric (ν_1) and antisymmetric (ν_3) stretches in bare CH_4 are shown by the dotted vertical lines. The y-axis shows the normalized photofragment yield.

$3.1.1 \quad \mathrm{Zr}^+(\mathrm{CH}_4)(\mathrm{Ar})$

The $[ZrCH_4]^+$ ion could be any one of several isomers, all intermediates in the Zr^+ + CH_4 reaction. So, before assigning the spectrum of this ion, it is essential to discuss the potential energy surface (PES) for the reaction, which is shown in Figure 2. These results are very similar to those of Armentrout *et al.*, which were at the B3LYP/HW+6-311++G(3df,3p) level. ¹⁸ The Zr^+ cation and $Zr^+(CH_4)$ entrance channel complex both have

Table 2: Calculated bond dissociation energies (BDE) of $Zr^+(CH_4)_{1-2}(Ar)$, $ZrCH_2^+(CH_4)_{0-1}(H_2)(Ar)$, and $Zr^+(CH_4)_{3-4}{}^a$

Species	S^b	kJ/mol	cm^{-1}
Zr^+ – CH_4	4	57.2	4782
$\operatorname{Zr^+(CH_4)}$ -Ar	4	29.8	2488
$\operatorname{ZrCH_2^+(H_2)} - \operatorname{Ar}$	2	32.2	2688
$\operatorname{ZrCH_2}^+(\operatorname{Ar}) - \operatorname{H_2}$	2	44.6	3730
$\operatorname{Zr}^+(\operatorname{CH}_4) - \operatorname{CH}_4$	4	58.6	4902
$\mathrm{Zr}^+(\mathrm{CH}_4)_2\mathrm{-Ar}$	4	1.6	133
$\operatorname{ZrCH_2^+}(\operatorname{CH_4})(\operatorname{H_2}) - \operatorname{Ar}$	2	9.6	804
$\operatorname{ZrCH_2^+}(\operatorname{CH_4})(\operatorname{Ar}) - \operatorname{H_2}$	2	21.3	1779
$\operatorname{ZrCH}_{2}^{+}(\operatorname{H}_{2})(\operatorname{Ar}) - \operatorname{CH}_{4}$	2	41.1	3434
$\overline{\operatorname{Zr}^+(\operatorname{CH}_4)_2 - (\operatorname{CH}_4)}$	4	14.0	1171
$\operatorname{Zr}^{+}(\operatorname{CH}_{4})_{3} - (\operatorname{CH}_{4})$	4	24.4	2043

^aB3LYP/aug-cc-pVTZ level of theory, at zero Kelvin. ^bSpin multiplicity

a quartet ground state. However, the minimum energy path involves a quartet to doublet crossing 57 prior to the transition state for hydrogen abstraction, at an energy of -16.6 kJ/mol, and the rest of the transition states, intermediates, and products are doublets. The [H-Zr-CH₃]⁺ insertion intermediate is the most stable species along the reaction pathway. Then, abstraction of a second hydrogen is more likely to form $(H_2)ZrCH_2^+$ rather than $(H)_2ZrCH_2^+$ as it has a significantly lower barrier. Formation of $ZrCH_2^+ + H_2$ products is predicted to

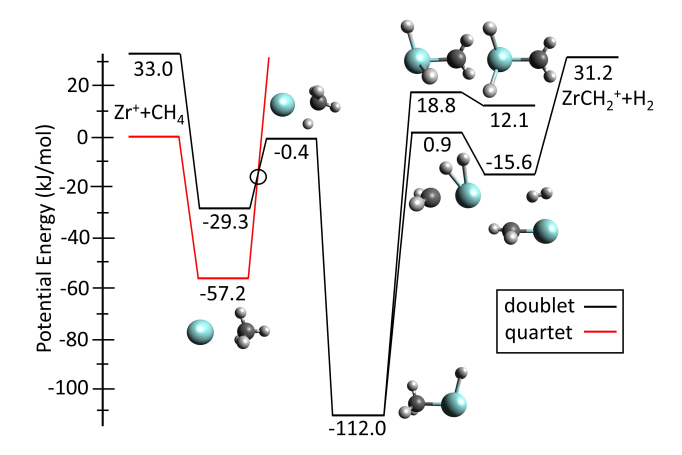


Figure 2: Potential energy surface for ${\rm Zr}^+$ + ${\rm CH_4}$ calculated using B3LYP/aug-cc-pVTZ.

be endothermic by 31.2 kJ/mol, which is somewhat higher than the experimental value of 13 ± 5 kJ/mol kJ/mol. ^{18,19} The calculation predicts that there are no barriers along the reaction path above this endothermicity, in agreement with experiment. ¹⁸ As noted earlier, the M11L functional predicts stronger Zr⁺-L bonds, so the barriers are lower and the overall reaction is predicted to be 9.7 kJ/mol exothermic, as shown in Table S1. In our experiment, the reaction is taking place in the presence of buffer gas (He or He/Ar). Collisions with the buffer gas can remove energy from the ions, leading to intermediates being trapped.

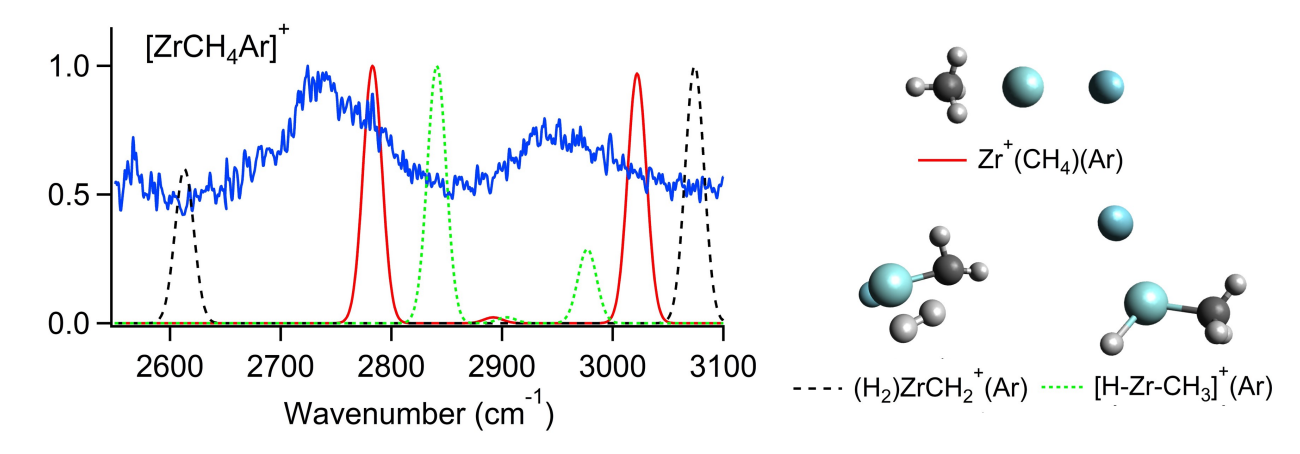


Figure 3: Experimental photodissociation spectrum (blue), simulated spectra of three low lying isomers and optimized geometries of $[ZrCH_4Ar^+]$ at the B3LYP/aug-cc-pVTZ level of theory.

No photodissociation is observed for $Zr^+(CH_4)$. Our calculations estimate a CH_4 binding energy of 57.2 kJ/mol (4782 cm⁻¹) which requires two photons to dissociate and IRMPD is inefficient for molecules this small, as shown by studies of $PtCH_2^+$. ⁴⁴ Table 2 shows the calculated binding energies at the B3LYP/aug-cc-pVTZ level and the energies and geometries discussed below are all at this level of theory. The binding energies for M11L are generally higher than those using B3LYP and are shown in Table S3. Zr^+ has a quartet ground state, and the ground state remains a quartet with the addition of CH_4 and Ar. Ar is predicted to be bound to $Zr^+(CH_4)$ by only 2488 cm⁻¹, so an Ar tag is used to obtain the spectrum. The spectra are sensitive to whether the CH_4 binds with η^2 hydrogen coordination, where two hydrogens point toward the metal, or η^3 , where three hydrogens point toward the metal.

Often, the coordination is intermediate between η^2 and η^3 . In these cases, it is useful to specify the angle between the Zr, C, and the hydrogen farthest away from the metal. Then, η^3 coordination gives $\angle \text{Zr-C-H}$ of 180° and η^2 gives ~ 124 °.

For $Zr^+(CH_4)(Ar)$, the calculations predict the Ar-Zr-C atoms are collinear and the CH_4 has η^3 hydrogen coordination ($\angle Zr-C-H=180^\circ$). The computed Zr-C bond length is 2.509 Å, which is 0.011 Å longer than in the untagged complex. The untagged and tagged simulated spectra predict similar peak positions (≤ 6 cm⁻¹ shifts) for the C-H stretches, confirming that the Ar only has a small effect on the spectrum.

The experimental and simulated spectra of Zr⁺(CH₄)(Ar) are shown in Figure 3. In the simulated spectrum, the peak at 2783 cm⁻¹ is the symmetric proximate C–H stretch and the peak at 3022 cm⁻¹ is the free C–H stretch on the distal hydrogen. The other C–H stretches are predicted to be much weaker. The experimental peak positions are more red shifted than the simulation predicts, with two broad peaks around 2730 and 2950 cm⁻¹. The symmetric C–H stretch is red shifted 187 cm⁻¹ from the value in bare CH₄ (2917 cm⁻¹). There is some dissociation throughout the experimental spectrum, likely due to absorption to an excited electronic state, so the baseline is not at zero.

There is a small, but reproducible, peak observed at 2567 cm⁻¹. It does not correspond to any fundamental vibrations of $Zr^+(CH_4)(Ar)$. There are two possible assignments for this peak. It could be due to bend overtones, which in bare CH_4 are $2\nu_4$ =2612 cm⁻¹ and $2\nu_2$ =3062 cm⁻¹.⁵⁸ The $2\nu_4$ bend overtone has been observed in the spectra of $Cu^+(CH_4)(Ar)_2^{35}$ and $F^-(CH_4)_n$.⁵⁹ The $2\nu_4$ overtones in those complexes are above 2600 cm⁻¹ and gain intensity from Fermi resonance with the lowest frequency C–H stretch.³⁵ However, in $Zr^+(CH_4)(Ar)$, the peak is at significantly lower wavenumber and it is ~150 cm⁻¹ below the lowest frequency C–H stretch, so it is less likely to mix and donate intensity to it.

The second, more likely, possibility is that this peak is due to the Ar-tagged exit channel complex, $(H_2)ZrCH_2^+(Ar)$. In this ion, the carbene undergoes an agostic distortion, so one C-H stretch is at very low wavenumber; this has been seen in $TaCH_2^+$ and WCH_2^{+} .

Similarly, reaction of laser-ablated neutral Zr atoms with methane in a cryogenic matrix forms $(H_2)ZrCH_2$, in which the agostic interaction has been characterized by vibrational spectroscopy in the fingerprint region. ^{60,61} Subsequent calculations confirm that the neutral $(H_2)ZrCH_2$ complexes have the most effective agostic interaction among second-row transition metals. ⁶² This happens because of the well developed double bond formed between the metal and carbon atom in conjunction with the metal's empty or half empty valence orbitals that can act as electron acceptors. In $(H_2)ZrCH_2^+(Ar)$ the carbene Zr-C-H angles are 162 and 86°, and the C-H stretches are predicted at 2613 and 3074 cm⁻¹ (Figure 3),consistent with the observed peak at 2567 cm⁻¹. No loss of H_2 upon photodissociation was observed for any of the complexes. However, the BDE of Ar is less than H_2 so the complex would preferentially lose Ar instead of H_2 . The predicted H-H bond length in the complex is 0.804 Å, which is 0.061 Å longer than in bare H_2 . ¹⁸ As a result, the H_2 stretch is calculated to be at 3290 cm⁻¹, which is red shifted \sim 900 cm⁻¹ from its value in free H_2 . Experiments to measure this vibration in the $Zr^+(CH_4)_2$ and $Zr^+(CH_4)_2(Ar)$ complexes will be discussed in the next section.

As the $[H-Zr-CH_3]^+$ insertion intermediate is the most stable species along the Zr^+ + CH_4 reaction path, it is likely that it is also produced and Ar tagged. Unfortunately, the calculated spectrum of $[H-Zr-CH_3]^+(Ar)$ in this wavelength region primarily consists of a peak at 2841 cm⁻¹, which is near the 2783 cm⁻¹ peak calculated for $Zr^+(CH_4)(Ar)$. The calculated intensities are very similar (Figure 3). This suggests that $[H-Zr-CH_3]^+(Ar)$ could account for the shoulder near 2780 cm⁻¹ in the experimental spectrum; however, it is difficult to tell for certain if this complex is present as the C-H stretches for the two isomers are at similar wavenumber and overlap. In summary, in the experimental spectrum, there is evidence for the entrance and exit channel complexes, $Zr(CH_4)^+(Ar)$ and $(H_2)ZrCH_2^+(Ar)$, and possibly of the insertion intermediate $[H-Zr-CH_3]^+(Ar)$ being produced.

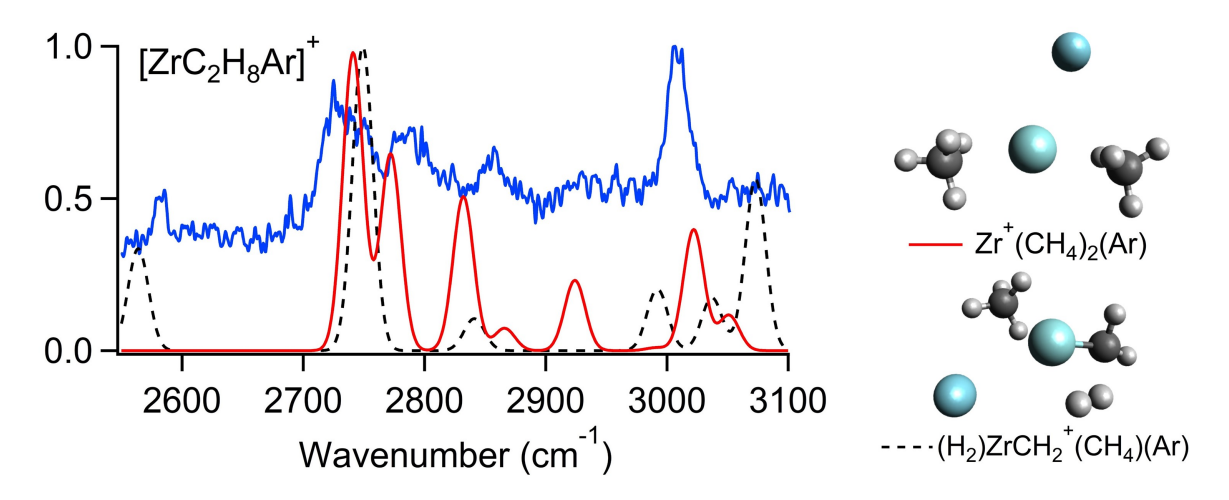


Figure 4: Experimental photodissociation spectrum (blue), simulated spectra of two low lying isomers and optimized geometries of $[ZrC_2H_8Ar^+]$ at the B3LYP/aug-cc-pVTZ level of theory.

$3.1.2 ext{ } ext{Zr}^+(CH_4)_2(Ar)$

The spectrum of $Zr^+(CH_4)_2$ was measured both with and without an Ar tag. The untagged spectrum (Figure S3) is due to infrared multiple photon dissociation (IRMPD), as the CH_4 is predicted to be bound by 4902 cm⁻¹ and so needs more than one photon to dissociate. It has two broad peaks around 2770 and 2994 cm⁻¹. There may be a peak at 2582 cm⁻¹ but the spectrum is noisy in this region because of low signal and laser power. The spectrum of $Zr^+(CH_4)_2(Ar)$ is much sharper and has peaks at 2582, 2725, 2783, 2857, and 3006 cm⁻¹ (Figure 4).

In the untagged molecule the C–Zr–C are collinear, and the CH₄ have η^3 coordination, with $r_{Zr-C}=2.487$ Å. The optimized geometry of the Ar tagged molecule has C_s symmetry and \angle C–Zr–C is bent to 161°. It has \angle C–Zr–Ar=79.8° and 119.4° with one CH₄ binding almost η^3 (\angle Zr–C–H=171°; $r_{Zr-C}=2.527$ Å) and the other closer to η^2 (\angle Zr–C–H=139°; $r_{Zr-C}=2.654$ Å).

The simulated spectrum of $Zr^+(CH_4)_2$ (shown in Figure S3) is very similar to that of $Zr^+(CH_4)$, with intense peaks at 2771 and 3028 cm⁻¹ due to the symmetric proximate C–H stretch and the free distal C–H stretch, respectively. The addition of the Ar makes the

geometry less symmetrical, which is reflected in the spectrum. The η^3 and η^2 methanes are red shifted to a different extent which leads to more unique C–H stretches and peaks in the spectrum. The series of peaks in the simulation are the symmetric proximate C–H stretch of the η^2 (2740 cm⁻¹) and η^3 (2772 cm⁻¹) methanes and the antisymmetric η^2 (2832 cm⁻¹) and η^3 (2866 and 2924 cm⁻¹) stretch. The peaks at 3022 and 3051 cm⁻¹ are the distal free C–H stretch of the η^3 methane and the distal antisymmetric C–H stretch on the η^2 CH₄, respectively.

The peak at 2582 cm⁻¹ could again be due to either the $2\nu_4$ bend overtone or to an $(H_2)ZrCH_2^+(CH_4)(Ar)$ exit channel complex, whose simulated spectrum and geometry are shown in Figure 4. The $\rm H_2$ stretch is predicted to be at 3343 cm⁻¹ and to be very intense, so additional experiments were done from $3300-3700~\mathrm{cm}^{-1}$ to look for this vibration. In order to observe small amounts of fragment ions, and to measure all dissociation pathways simultaneously, these experiments measured the difference between mass spectra with the IR laser on and off at each IR wavelength. For $Zr^+(CH_4)_2$, no H_2 loss was observed, however, we are not sensitive to this channel because the small fragment signal lies too close to the much larger parent signal. There is some $\mathrm{CH_4}$ loss, and it peaks at 3355 $\mathrm{cm^{-1}}$, as shown in Figure S4. This peak increases in intensity with lower backing pressure and higher laser power. This leads to hotter conditions where the ions are more likely to react to form intermediates and exit channel complexes. The same set of experiments were carried out with the Ar tagged complex. A small peak was observed on top of background dissociation around 3325 cm⁻¹ while monitoring Ar loss, the only channel observed. The simulated H₂ peak position for $(\mathrm{H_2})\mathrm{ZrCH_2}^+(\mathrm{CH_4})(\mathrm{Ar})$ is 3426 cm⁻¹ so the observed peak is 100 cm⁻¹ more red shifted than predicted.

In addition, the intensity of the peak at 2582 cm⁻¹ was also found to increase with low backing pressure and high laser power. In contrast, the 2780 cm⁻¹ peak, which is due to the entrance channel complex, was found to decrease with increasing laser power. This behavior confirms that the peak at 2582 cm⁻¹ is due to an exit channel complex. In summary, most of

the spectrum shown in Figure 4 is due to $Zr^+(CH_4)_2(Ar)$, but the small peak at 2582 cm⁻¹ is due to $(H_2)ZrCH_2^+(CH_4)(Ar)$, which also has a peak at 3325 cm⁻¹.

$3.1.3 \text{ Zr}^+(\text{CH}_4)_3$

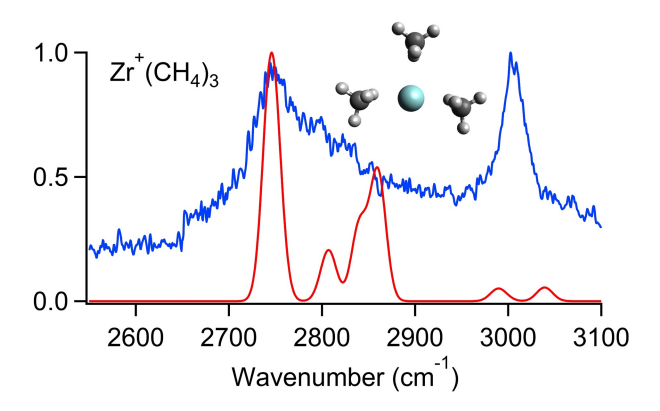


Figure 5: Experimental photodissociation spectrum (blue), simulated spectrum (red), and optimized geometry of $\mathrm{Zr}^+(\mathrm{CH}_4)_3$ at the B3LYP/aug-cc-pVTZ level of theory.

The experimental spectrum of $Zr^+(CH_4)_3$ (Figure 5) has two intense peaks, at 2747 and 3002 cm⁻¹. The third CH_4 is calculated to be bound by 14.2 kJ/mol (1189 cm⁻¹), which is much weaker than the first two ligands. This decrease is also seen in $M^+(CH_4)_n$ complexes of M=Mn, 32 Fe, 33 Co, 34 Ni, 34 Cu, 35 Ag, 35 and Au. 36 The optimized geometry has C_s (nearly C_{2v}) symmetry and two different methane binding orientations. Two are nearly η^2 ($\angle Zr-C-H=143^\circ$; $r_{Zr-C}=2.637$ Å) and one is η^2 ($\angle Zr-C-H=125^\circ$; $r_{Zr-C}=2.866$ Å) with $\angle C-Zr-C=96^\circ$ x2 and 167°.

The breadth of the 2747 cm⁻¹ peak and its tailing to higher cm⁻¹ suggest that the CH₄ can inter-convert readily. The first two CH₄ bind strongly by maintaining s-d hybridization, so the third CH₄ is further from the metal center and weakly bound. According to theory, this is slightly more favorable for $\text{Zr}^+(\text{CH}_4)_3$ than having three equivalent bonds where the first two are weakened to strengthen the third.⁶³

The peaks in the simulation are the symmetric C–H stretch of the nearly η^2 CH₄ (2746 cm⁻¹) and the η^2 CH₄ (2806 cm⁻¹) and the antisymmetric C–H stretch of the nearly η^2 CH₄ (2840 cm⁻¹) and the η^2 CH₄ (2860 cm⁻¹). The weak peaks in the simulation at 2990

and 3039 cm⁻¹ are the distal symmetric and antisymmetric C–H stretches of the nearly η^2 CH₄.

$3.1.4 \text{ Zr}^+(\text{CH}_4)_4$

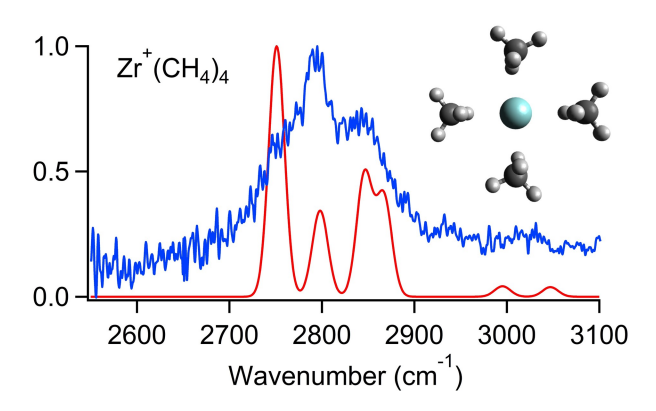


Figure 6: Experimental photodissociation spectrum (blue), simulated spectrum (red), and optimized geometry of $Zr^+(CH_4)_4$ at the B3LYP/aug-cc-pVTZ level of theory.

The fourth CH_4 is calculated to be bound by 24.4 kJ/mol (2043 cm⁻¹), which is more strongly bound than the third CH_4 ; this has also been observed in $Ti^+(CH_4)_n$ complexes.⁶³ This is explained by the energy associated with the loss of s-d hybridization of the first two CH_4 , which is shared between the third and fourth CH_4 .⁶³ This is usually not the case for late transition metals, where the fourth CH_4 binds more weakly than the third. The experimental spectrum (Figure 6) shows an intense peak at 2795 and a second, less intense peak at 2834 cm⁻¹.

The optimized geometry of $\operatorname{Zr}^+(\operatorname{CH}_4)_4$ is slightly distorted square planar with $\angle \operatorname{C-Zr-C}$ bond angles of 89 or 90°. The CH_4 bind with η^2 coordination at two bond lengths, $r_{Zr-C}=2.679$ and 2.844 Å. The two closer CH_4 are bent away from the metal slightly and have $\angle \operatorname{Zr-C-H} = 135^\circ$ rather than 124°. The simulated spectrum shows the symmetric and antisymmetric stretches of the nearer (2751 cm⁻¹ and 2847 cm⁻¹) and more distant (2798 cm⁻¹ and 2865 cm⁻¹) CH_4 . Calculations predict that the square planar structure is a transition state and lies only 129 cm⁻¹ above the distorted square planar minima. It is possible that, due to the low barrier, intermediate structures also contribute to the spectrum, and would tend to

lead to higher absorption near 2770 cm⁻¹. Unlike the smaller clusters, there is no peak near 3000 cm⁻¹, indicating that structures with η^3 hydrogen coordination do not contribute to the spectrum.

3.2 Methane Activation Products

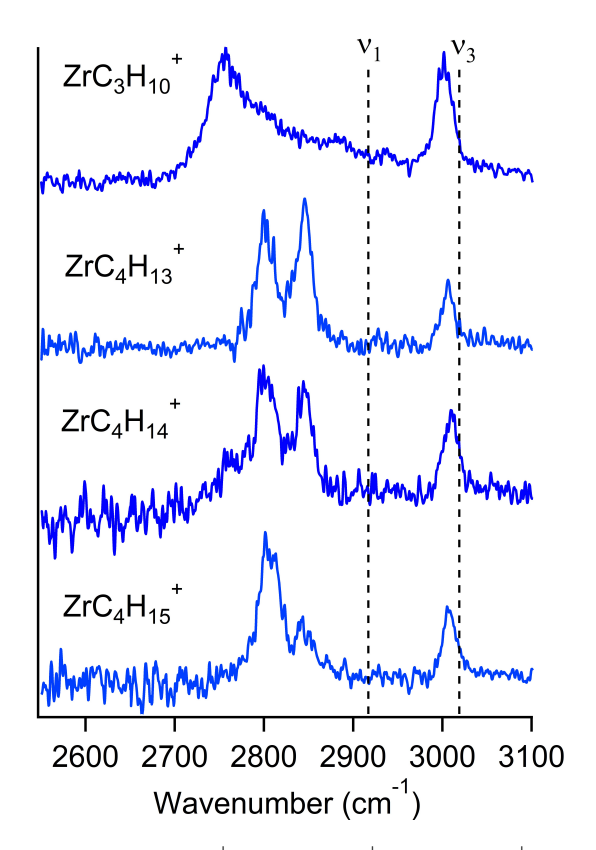


Figure 7: Vibrational spectra of ${\rm ZrC_3H_{10}}^+$, ${\rm ZrC_4H_{13}}^+$, ${\rm ZrC_4H_{14}}^+$, and ${\rm ZrC_4H_{15}}^+$ in the C–H stretching region (2550-3100 cm⁻¹). The y-axis shows the normalized photofragment yield. The vertical lines indicate the positions of the symmetric (ν_1) and antisymmetric (ν_3) C–H stretches in bare CH₄.

Sequential reaction of Zr^+ with methane also leads to $ZrC_3H_{10}^+$, which corresponds to loss of H_2 from $Zr^+(CH_4)_3$, and to $ZrC_4H_n^+$ (n=13-15), loss of H, H_2 , and $H_2 + H$ from $Zr^+(CH_4)_4$. The structures of the reaction products are determined by comparing calculated vibrational spectra of possible isomers to the measured spectra. The spectra, shown in Figure 7, show one or two peaks that are red shifted from the symmetric C-H stretch in CH_4 (ν_1 =2917 cm⁻¹), and a peak slightly red shifted from the antisymmetric stretch (ν_3 =3019

cm $^{-1}$). The ZrC₃H₁₀⁺ spectrum looks similar to the Zr⁺(CH₄)₃ spectrum, while the spectra of ZrC₄H₁₃⁺, ZrC₄H₁₄⁺, and ZrC₄H₁₅⁺ are similar to each other, with the intensity of the higher energy peak of the doublet increasing as more hydrogen atoms are lost. For each of these complexes, calculations were carried out for multiple isomers in the doublet and quartet or singlet, triplet, and quintet spin states. The results at the B3LYP/aug-cc-pVTZ level are summarized in Table 3. Results using the M11L functional are in Table S5. Both functionals predict isomers with very similar geometries and similar relative energies. The simulated spectra shown below all use the B3LYP functional. Simulations with the M11L functional are in the SI (Figures S5, S6, S8, and S9). They provide a better match to the experimental spectra for the reaction products. However, this functional is significantly worse at predicting spectra of the entrance channel complexes. These reactions, except for the loss of H, are exothermic at the B3LYP/aug-cc-pVTZ level of theory (Table 4) and all four reactions are exothermic at the M11L/aug-cc-pVTZ level (Table S5). The spectra, structures, and corresponding simulations of the reaction products will be discussed in the following sections.

$3.2.1 \quad \text{ZrC}_3 \text{H}_{10}^{+}$

 ${\rm ZrC_3H_{10}}^+$ corresponds to dehydrogenation of ${\rm Zr}^+({\rm CH_4})_3$. Its spectrum, shown in Figure 8, consists of an intense peak at 2757 cm⁻¹ with a shoulder to higher energy and an equally intense peak at 3001 cm⁻¹. The isomers investigated include a zirconium carbene cation with two methane molecules, ${\rm ZrCH_2}^+({\rm CH_4})_2$; a zirconium dimethyl cation with a methane molecule, ${\rm Zr(CH_3)_2}^+({\rm CH_4})$; and a zirconium cation with methane and ethane where the ethane is either linear or side-on to the metal, ${\rm Zr}^+({\rm C_2H_6})({\rm CH_4})$, in the doublet and quartet states. The calculations, shown in Table 3, predict that doublet ${\rm Zr(CH_3)_2}^+({\rm CH_4})$ is the lowest energy isomer, with ${\rm ZrCH_2}^+({\rm CH_4})_2$ 94.0 kJ/mol higher in energy. The corresponding quartet states are all at significantly higher energy. The doublet and quartet states of ${\rm Zr}^+({\rm C_2H_6})({\rm CH_4})$ have relative energies of 133 kJ/mol and 131 kJ/mol (linear) and 135

Table 3: Calculated bond dissociation energies (BDE) for loss of $\mathrm{CH_4}$ and relative energies (E_{rel}) of possible isomers for the reaction products $\mathrm{ZrC_3H_{10}}^+$, $\mathrm{ZrC_4H_{13}}^+$, $\mathrm{ZrC_4H_{14}}^+$, and $\mathrm{ZrC_4H_{15}}^+$

G :	S^b	BDE		E_{rel}	
Species		$\overline{\mathrm{kJ/mol}}$	cm^{-1}	$\overline{\mathrm{kJ/mol}}$	cm^{-1}
$\mathrm{ZrC_3H_{10}}^+$		·		·	
$\operatorname{Zr}(\operatorname{CH}_3)_2^+(\operatorname{CH}_4)$	2	81.4	6802	0.0	0
$\operatorname{ZrCH}_{2}^{+}(\operatorname{CH}_{4})_{2}$	2	59.1	4940	94.0	7862
$\mathrm{Zr}^+(\mathrm{C}_2\mathrm{H}_6)(\mathrm{CH}_4)^d$	4	55.0	4599	125.8	10514
$\operatorname{Zr^+}(\operatorname{C_2H_6})(\operatorname{CH_4})^c$	4	58.1	4856	131.4	10982
$\mathrm{Zr}^+(\mathrm{C_2H_6})(\mathrm{CH_4})^c$	2	78.7	6582	133.3	11139
$\operatorname{Zr}^+(\operatorname{C}_2\operatorname{H}_6)(\operatorname{CH}_4)^d$	2	74.1	6193	134.5	11242
$\overline{\mathrm{ZrC_4H_{13}}^+}$					
$\operatorname{Zr}(\operatorname{CH}_3)_3^+(\operatorname{CH}_4)$	1	59.0	4932	0.0	0
$\operatorname{ZrCH}_2(\operatorname{CH}_3)^+(\operatorname{CH}_4)_2$	1	52.9	4421	113.8	9514
$\mathrm{HZrCH_2}(\mathrm{CH_3})_2^+(\mathrm{CH_4})$	1	1.0	80	124.8	10434
$\operatorname{ZrCH}^+(\operatorname{CH}_4)_3$	1	52.3	4370	211.9	17714
$\overline{\mathrm{ZrC_4H_{14}}^+}$					
$Zr(CH_3)_2^+(CH_4)_2 (A)^e$	2	19.7	1646	0.0	0
$\operatorname{Zr}(\operatorname{CH}_3)_2^+(\operatorname{CH}_4)_2(\operatorname{B})^e$	2	13.5	1130	6.2	516
$Zr(CH_3)_2^+(CH_4)_2 (C)^e$	2	7.9	664	11.7	982
$\operatorname{Zr}(\operatorname{CH}_3)_2^+(\operatorname{CH}_4)_2^-(\operatorname{D})^e$	2	7.0	586	12.7	1059
$\operatorname{ZrCH_2^+}(\operatorname{CH_4})_3$	2	15.2	1273	98.5	8234
$\operatorname{Zr}^+(\operatorname{C}_2\operatorname{H}_6)(\operatorname{CH}_4)_2{}^d$	2	7.8	656	146.3	12232
$\mathrm{ZrC_4H_{15}}^+$					
$\operatorname{ZrCH_3^+}(\operatorname{CH_4})_3$	3	19.4	1623	0.0	0
$\mathrm{HZrCH_2}^+(\mathrm{CH_4})_3$	1	20.2	1691	2.9	243
$\operatorname{ZrCH_3^+}(\operatorname{CH_4})_3$	1	0.9	74	48.8	4080
$HZrCH_2^+(CH_4)_3$	3	25.3	2115	112.6	9410

 $^a\mathrm{Calculations}$ are done at zero Kelvin at the B3LYP/aug-cc-pVTZ level of theory. $^b\mathrm{Spin}$ multiplicity. $^c\mathrm{C}_2\mathrm{H}_6$ is collinear with the metal. $^d\mathrm{C}_2\mathrm{H}_6$ is side-on to the metal. $^e\mathrm{A-D}$ refer to different isomers.

Table 4: Thermodynamics of the reactions for loss of H, H₂, and H+H₂ a

Reaction	kJ/mol	cm^{-1}
$\operatorname{Zr}^+ + 3 \operatorname{CH}_4 \longrightarrow \operatorname{Zr}(\operatorname{CH}_3)_2^+(\operatorname{CH}_4) + \operatorname{H}_2$	-191.1	-15974
$\operatorname{Zr}^+ + 4 \operatorname{CH}_4 \longrightarrow \operatorname{ZrCH}_3^+(\operatorname{CH}_4)_3 + \operatorname{H}$	42.1	3515
$\longrightarrow HZrCH_2^+(CH_4)_3 + H$	45.0	3758
$\longrightarrow \operatorname{Zr}(\operatorname{CH}_3)_2^+(\operatorname{CH}_4)_2^+ + \operatorname{H}_2^-$	-210.8	-17620
$\longrightarrow \operatorname{Zr}(\operatorname{CH}_3)_3^+(\operatorname{CH}_4) + \operatorname{H}_2 + \operatorname{H}$	-43.3	-3620

^aCalculated at the B3LYP/aug-cc-pVTZ level of theory, at zero Kelvin.

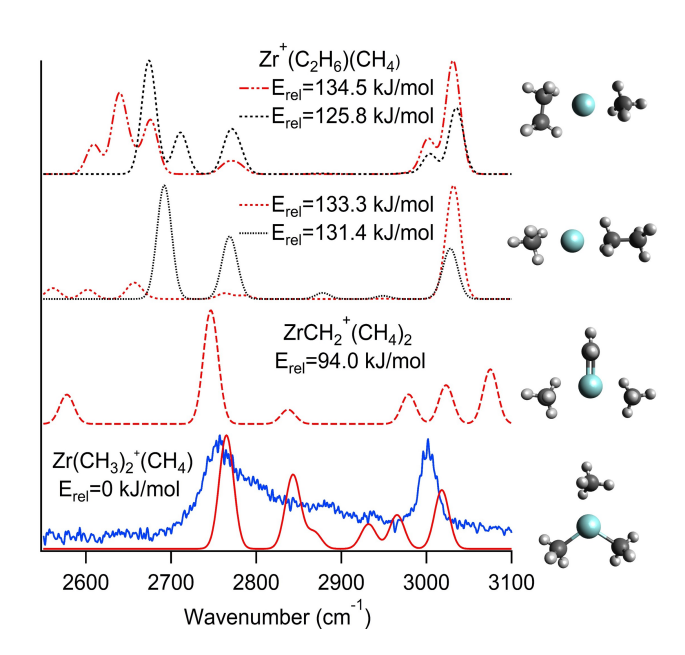


Figure 8: Experimental photodissociation spectrum (blue), scaled simulated spectra (red = doublet and black = quartet) with relative energies and optimized geometries of doublet isomers of ${\rm ZrC_3H_{10}}^+$ at the B3LYP/aug-cc-pVTZ level of theory.

kJ/mol and 126 kJ/mol (side-on).

The simulated spectra and corresponding geometries are shown in Figure 8. Although the ethane complexes all have an intense peak near 3030 cm⁻¹, they fail to reproduce the 2757 cm⁻¹ peak and predict multiple peaks below 2700 cm⁻¹, which are not observed. Although the spectrum of $ZrCH_2^+(CH_4)_2$ has an intense peak at 2757 cm⁻¹, it also has a peak at 2577 cm⁻¹ and a triplet around 3000 cm⁻¹ which do not match the experiment.

The observed spectrum is due to $\text{Zr}(\text{CH}_3)_2^+(\text{CH}_4)$. Its simulation best matches the experiment and is the most stable isomer by 94 kJ/mol (Table 3). The carbon and zirconium atoms are nearly in the same plane. The methane binds in an almost η^3 orientation ($\angle \text{Zr}-\text{C}-\text{H}=166^\circ$; $r_{Zr-C}=2.580$ Å). The two methyl groups have $r_{Zr-C}=2.160$ Å and $\angle \text{C}-\text{Zr}-\text{C}=110^\circ$. The peaks in the simulated spectrum are the proximate symmetric C-H stretch of CH₄ (2765 cm⁻¹), the symmetric C-H stretches of the -CH₃ groups (2843 cm⁻¹), the antisymmetric C-H stretch of CH₄ (2867 cm⁻¹), and the free distal C-H stretch of CH₄ (3018 cm⁻¹). The antisymmetric C-H stretches of -CH₃ (2932 cm⁻¹) and CH₄ (2965 cm⁻¹) are predicted to be weak and are not seen in the experimental spectrum.

The simulated spectrum and geometry of the lowest energy isomer using M11L is shown in Figure S5. The M11L functional predicts the relative peak intensities better than B3LYP. The M11L geometry has the methane closer to the metal ($r_{Zr-C}=2.519$ Å) and closer to η^3 (\angle Zr-C-H = 176°) than B3LYP. This could be the reason for the better predicted spectrum, as an intense peak near 3000 cm⁻¹ is characteristic of an η^3 methane.

$3.2.2 \quad {\rm ZrC_4H_{13}}^+$

The $\operatorname{ZrC}_4H_{13}^+$ molecule corresponds to loss of H_2+H from $\operatorname{Zr}^+(\operatorname{CH}_4)_4$. The spectrum, shown in Figure 9, consists of a doublet with two intense peaks at 2800 and 2845 cm⁻¹ and a less intense peak at 3006 cm⁻¹. The isomers considered include a trimethyl zirconium cation with a methane molecule, $\operatorname{Zr}(\operatorname{CH}_3)_3^+(\operatorname{CH}_4)$; a dimethyl hydrido-zirconium carbene cation with a methane molecule, $\operatorname{HZrCH}_2(\operatorname{CH}_3)_2^+(\operatorname{CH}_4)$; a methyl zirconium carbene cation with

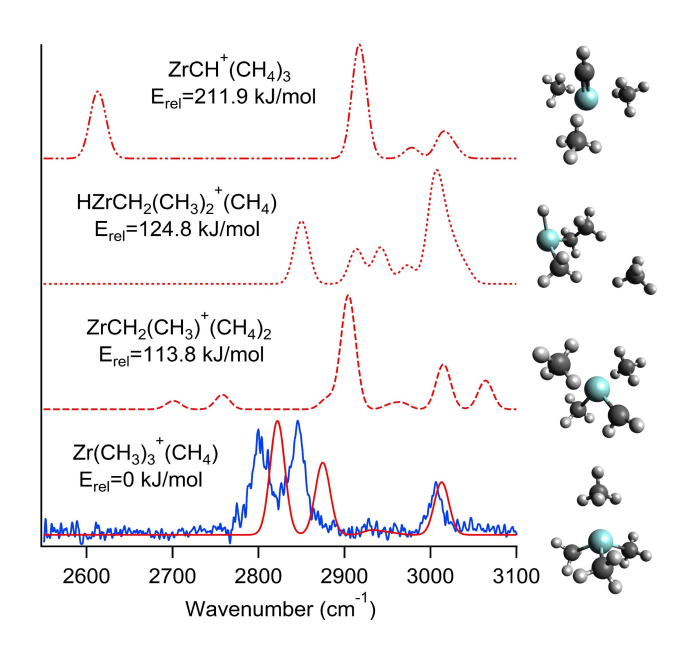


Figure 9: Experimental photodissociation spectrum (blue), scaled simulated spectra (red) with relative energies, and optimized geometries of $\rm ZrC_4H_{13}^{+}$ isomers at the B3LYP/aug-cc-pVTZ level of theory.

two methane molecules, $ZrCH_2(CH_3)^+(CH_4)_2$; and a zirconium carbyne cation with three methane molecules, $ZrCH^+(CH_4)_3$, in the singlet, triplet, and quintet states. For all of the species, the singlets are calculated to lie at least 100 kJ/mol below the other spin states.

The simulated spectra of the singlet states are shown in Figure 9. The $HZrCH_2(CH_3)_2^+(CH_4)$, $ZrCH_2(CH_3)^+(CH_4)_2$, and $ZrCH^+(CH_4)_3$ isomers have relatively high energies and their simulated spectra do not have a doublet around 2800 cm⁻¹. The spectrum of the $Zr(CH_3)_3^+(CH_4)$ isomer, however, does have a doublet and provides an excellent match to the experimental spectrum. It is the most stable isomer by 113.8 kJ/mol (Table 3).

The geometry of this isomer is approximately tetrahedral with $\angle CH_3-Zr-CH_3=107^\circ$ and $\angle CH_3-Zr-CH_4=112^\circ$. The three methyl groups have $r_{Zr-C}=2.176$ Å and the methane has $r_{Zr-C}=2.574$ Å and η^3 hydrogen coordination. The imino-enamido trimethyl zirconium polymerization pre-catalysts synthesized by Fontaine *et al.*²² have a similar geometry, with slightly longer $r_{Zr-C}=2.234-2.260$ Å likely due to enhanced electron donation from the imino-enamido ligand. The low energy peak of the doublet, at 2822 cm⁻¹, corresponds to the symmetric C-H stretch of CH₄ and the high energy peak at 2874 cm⁻¹ is the symmetric

C-H stretch of the methyl groups. This later peak is fairly intense because there are three methyl groups contributing to the spectrum. The peak at 3006 cm⁻¹ corresponds to the free distal C-H stretch in CH₄. The antisymmetric stretches of the methane and the methyl groups are weak and are not observed in the experimental spectrum. The doublet in the experimental spectrum is about 30 cm⁻¹ more red shifted than is predicted by the simulated spectrum using B3LYP while the peak at 3006 cm⁻¹ is a good match with only a 6 cm⁻¹ shift.

Figure S6 shows the geometry and simulated vibrational spectrum of $Zr(CH_3)_3^+(CH_4)$ at the M11L level of theory. Using this functional, the predicted doublet peaks are only 5 and 12 cm⁻¹ less red shifted than the experimental peaks but the peak at higher wavenumber is high by 44 cm⁻¹. The geometry is very similar to that at B3LYP, with the CH_4 slightly closer to the metal $(r_{Zr-C}=2.553 \text{ Å})$.

$3.2.3 \quad ZrC_4H_{14}^{+}$

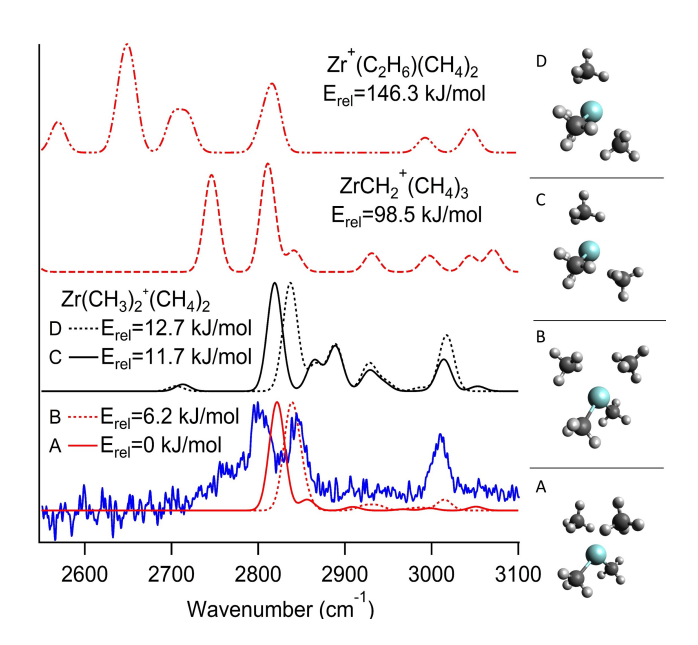


Figure 10: Experimental photodissociation spectrum (blue), scaled simulated spectra (red) with relative energies, and optimized geometries of $ZrC_4H_{14}^{+}$ at the B3LYP/aug-cc-pVTZ level of theory. Only the $Zr(CH_3)_2^+(CH_4)_2$ isomers are shown on the graph, the rest are shown in Table S9.

The $\operatorname{ZrC_4H_{14}^+}$ molecule corresponds to loss of $\operatorname{H_2}$ from $\operatorname{Zr^+(CH_4)_4}$. The experimental spectrum, shown in Figure 10, consists of a doublet at 2799 and 2844 cm⁻¹ and a peak at 3010 cm⁻¹. The peaks have shifted slightly from the $\operatorname{ZrC_4H_{13}^+}$ spectrum and the higher-energy peak of the doublet has decreased intensity relative to the lower-energy peak.

The geometries considered are a zirconium carbene cation with three methane molecules, $\operatorname{ZrCH}_2^+(\operatorname{CH}_4)_3$; a zirconium dimethyl cation with two methane molecules, $\operatorname{Zr}(\operatorname{CH}_3)_2^+(\operatorname{CH}_4)_2$; and a zirconium cation with an ethane and two methane groups, $\operatorname{Zr}^+(\operatorname{C}_2\operatorname{H}_6)(\operatorname{CH}_4)_2$, in the doublet and quartet states.

The simulated spectra of the doublet states are shown in Figure 10. The spectra of $Zr^+(C_2H_6)(CH_4)_2$ and $ZrCH_2^+(CH_4)_3$ do not match the experiment. They are also much higher in energy than $Zr(CH_3)_2^+(CH_4)_2$. The calculations predict four low-energy isomers of $Zr(CH_3)_2^+(CH_4)_2$ which differ in the distances and orientations of the CH_4 . They are shown in Figure 10 and are labeled A (lowest energy) to D (highest energy).

No single simulation predicts a doublet. However, if the spectra of the two lowest energy isomers, A and B, are plotted together they produce a doublet with a separation of 17 cm⁻¹ instead of the 45 cm⁻¹ observed in the experimental spectrum. The C and D isomers do as well, but they are high enough in energy that it is not likely they are extensively produced in the experiment. Complexes A and B are close to tetrahedral with two η^2 (\angle Zr-C-H = 126°; r_{Zr-C} =2.796 Å) and two η^3 (\angle Zr-C-H = 170°; r_{Zr-C} =2.748 Å) CH₄, respectively. The most intense peaks in the spectra are due to the CH₄ symmetric stretches and the simulations predict the η^2 symmetric C-H stretches to be more red shifted than the η^3 symmetric stretches. Isomer A also has a moderate-intensity peak at 2856 cm⁻¹ due to the symmetric stretch of the -CH₃ groups. This could also contribute to the higher-energy peak of the doublet. The calculations predict that the free distal stretch of an η^3 CH₄ and the distal antisymmetric stretch of an η^2 CH₄ contribute to the 3010 cm⁻¹ peak. The intensities in each simulation are scaled to the most intense peak in each individual simulation, so it can be hard to tell the relative intensities for each isomer. The unscaled intensities are plotted

in Figure S7.

A mixture of isomers with CH_4 hydrogen orientation ranging from η^2 to η^3 likely contribute to the spectrum, producing the doublet near 2800 cm⁻¹ and moderately intense peak at 3010 cm⁻¹. Another possibility is that the spectrum is from only one isomer and the doublet near 2800 cm⁻¹ is due to the CH_4 and $-CH_3$ symmetric stretches, as in $Zr(CH_3)_3^+(CH_4)$. Fermi resonance between these vibrations could cause the peaks to separate more (as in the experimental spectrum) and the $-CH_3$ symmetric stretch to gain intensity from the CH_4 symmetric stretch.

Figure S8 shows the simulated spectra and geometries of the two lowest energy isomers at the M11L level of theory. The results are similar to the B3LYP simulations, with each isomer having a major peak near 2800 cm^{-1} due to the CH₄ symmetric stretch.

$3.2.4 \quad \text{ZrC}_4 \text{H}_{15}^{+}$

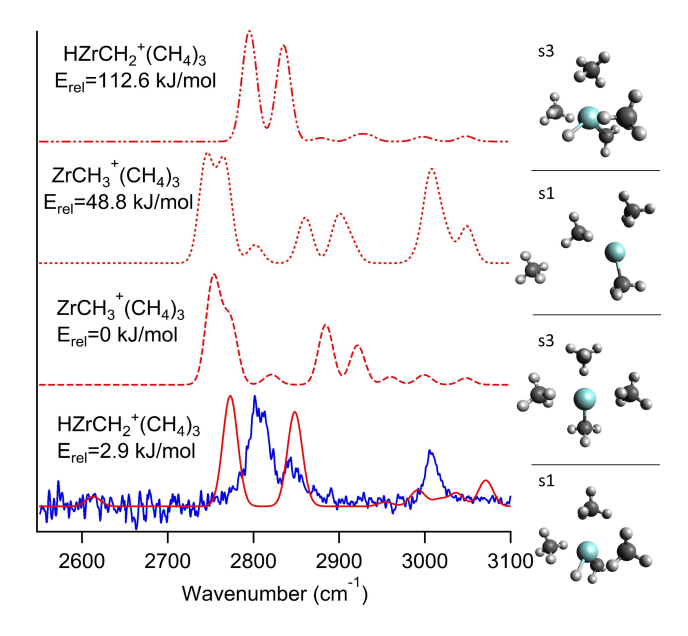


Figure 11: Experimental photodissociation spectrum (blue), scaled simulated spectra (red) with relative energies, and optimized geometries of $\rm ZrC_4H_{15}^{+}$ at the B3LYP/aug-cc-pVTZ level of theory. The s1 and s3 on the graph label the singlet and triplet spin states.

The $ZrC_4H_{15}^+$ molecule corresponds to loss of H atom from $Zr^+(CH_4)_4$. The spectrum consists of a doublet at 2801 and 2842 cm⁻¹ and a peak at 3005 cm⁻¹ (Figure 11). The

higher-energy peak of the doublet has now decreased substantially relative to the lowerenergy peak.

The isomers considered are a zirconium methyl cation with three methanes, $\operatorname{ZrCH}_3^+(\operatorname{CH}_4)_3$; and a hydrido-zirconium carbene cation with three methane groups, $HZrCH_2^+(CH_4)_3$, in the singlet, triplet, and quintet states. The simulations and geometries of the singlet and triplet states are shown in Figure 11. The quintets are at substantially higher energy. The spectrum of the $\mathrm{HZrCH_2}^+(\mathrm{CH_4})_3$ isomer in the triplet state has a nice doublet around 2800 cm⁻¹, but it is quite high in energy. The singlet state of $\operatorname{ZrCH}_3^+(\operatorname{CH}_4)_3$ is also high in energy. It is predicted to contain a second shell η^3 methane, which leads to the intense peak at 3008 cm⁻¹ in the simulation. The lowest energy isomer is the $\operatorname{ZrCH}_3^+(\operatorname{CH}_4)_3$ molecule in the triplet state, however, it is not a good match to the experimental spectrum, as the CH_4 ligands have η^2 coordination, leading to an intense peak at 2754 cm⁻¹. This peak is too red shifted from the experimental spectrum and the peaks around $3000~\mathrm{cm^{-1}}$ are weak. Based on the similarity in the spectra of $\operatorname{ZrC_4H_{13-15}}^+$, it is likely that $\operatorname{ZrC_4H_{15}}^+$ is $\operatorname{ZrCH_3}^+(\operatorname{CH_4})_3$ with the methanes η^3 . The functionals used, B3LYP and M11L, appear to slightly favor η^2 over η^3 methane coordination. Another possibility is that the spectrum is due to the $\mathrm{HZrCH_2}^+(\mathrm{CH_4})_3$ isomer in the singlet state, which is only 2.9 kJ/mol higher in energy. Although a good match to the experimental spectrum, it still does not capture the peak at 3005 cm⁻¹ well.

The $\mathrm{HZrCH_2}^+(\mathrm{CH_4})_3$ molecule is predicted to have an agostic carbene group and a hydrogen covalently bound to the metal. Two of the methane molecules are intermediate between η^2 and η^3 coordination with $\angle\mathrm{Zr-C-H} = 148^\circ$ ($r_{Zr-C}=2.655$ Å) and one is almost η^3 ($\angle\mathrm{Zr-C-H} = 166^\circ$; $r_{Zr-C}=2.801$ Å). The carbene carbon is almost perpendicular to the adjacent methane carbon atoms with an angle of 101°. The doublet in the simulated spectrum corresponds to the 148° (2773 cm⁻¹) and 166° (2849 cm⁻¹) methane symmetric C–H stretches. There are several weak peaks from 2950 to 3070 cm⁻¹ which correspond to the antisymmetric stretches of the methanes and the carbone C–H stretches.

The simulated spectrum of singlet $\mathrm{HZrCH_2}^+(\mathrm{CH_4})_3$ with the M11L functional (Figure

S9) provides a much better match to the experimental spectrum, with a doublet separated by only 42 cm⁻¹, at 2796 and 2838 cm⁻¹, and an intense peak at 3051 cm⁻¹. The doublet peaks are again due to the symmetric C–H stretches in the CH₄ ligands. The peak at 3051 cm⁻¹ corresponds to the antisymmetric C–H stretches in the CH₄ and a free C–H stretch on the CH₂ group. The M11L functional predicts the methanes to be closer to the metal and closer to η^3 (\angle Zr–C–H = 158°and 172°; r_{Zr-C} =2.601Å and 2.779Å). As shown in Table 4, production of HZrCH₂⁺(CH₄)₃ from sequential reaction of Zr⁺ with four methane molecules is predicted to be endothermic at the B3LYP/aug-cc-pVTZ level; however, it is predicted to be slightly exothermic using M11L (Table S5).

Armentrout and coworkers have studied the sequential reactions of Pt^+ and Ir^+ with methane, measuring the vibrational spectra of the reaction products in the fingerprint region using IRMPD at the FELIX free electron laser facility. For Pt^+ , the observed products are $Pt(CH_3)_2^+(CH_4)_{n-2}$ (n=2-4), ⁴⁴ paralleling our observation of $Zr(CH_3)_2^+(CH_4)_{n-2}$ (n=3-4). Ir^+ shows more extensive C-H activation, forming products such as $HIr(CH_3)_3^+$. ⁴⁷

The mechanism for forming the observed H and H_2 loss products is likely similar to that proposed for formation of $Ti(CH_3)_2^+(CH_4)$ by sequential reaction of Ti^+ with methane by Bowers and coworkers. 17,63 Clustering of Zr^+ with methanes produces $Zr^+(CH_4)_n$. As this reaction is quite exothermic, these clusters can contain substantial internal vibrational energy. Upon colliding with another methane molecule, the zirconium atom inserts into the methane C-H bond to form $[H-Zr-CH_3]^+(CH_4)_n$, which can lose a hydrogen atom to form $ZrCH_3^+(CH_4)_n$ or $HZrCH_2^+(CH_4)_n$. Alternatively, the $[H-Zr-CH_3]^+(CH_4)_n$ can react with another methane, inserting into a second C-H bond, and transiently forming $(H)_2Zr(CH_3)_2^+(CH_4)_n$. The hydrogens quickly combine to produce $(H_2)Zr(CH_3)_2^+(CH_4)_n$. Loss of H_2 forms $Zr(CH_3)_2^+(CH_4)_n$. $Zr(CH_3)_3^+(CH_4)_n$ is likely formed by insertion of $Zr(CH_3)_2^+(CH_4)_n$ into a methane C-H bond, followed by H atom loss.

4 Summary and Conclusions

Reaction of Zr^+ with methane produces $ZrC_nH_{4n}^+$ (n=1-4) ions as well as the C-H bond activation products $ZrC_3H_{10}^+$, $ZrC_4H_{13}^+$, $ZrC_4H_{14}^+$, and $ZrC_4H_{15}^+$. Photofragment spectroscopy is used to measure the IR vibrational spectra in the C-H stretching region (2550-3100 cm⁻¹) to determine the structure of the ions. The spectra are obtained by monitoring loss of Ar for the tagged complexes, $Zr^+(CH_4)_n(Ar)$ (n=1-2), and loss of CH_4 for the other ions. Simulated spectra based on calculations at the B3LYP/aug-cc-pVTZ level of theory are a good match for the complexes studied, however, the M11L functional does a better job at capturing the spectra of the reaction products, as shown in the SI. The geometries predicted using both functionals are very similar; however, M11L tends to predict that the CH_4 ligands are closer to Zr and have the hydrogen coordination closer to η^3 .

The spectra of the entrance channel complexes, $Zr^+(CH_4)_n$ (n=1-4), show peaks due to the symmetric and free distal C-H stretches of CH₄. The symmetric stretch is red shifted by 187, 192, 170, and 122 cm⁻¹ for n=1-4, relative to ν_1 =2917 cm⁻¹ in bare methane. The methane has η^3 hydrogen coordination in the smaller entrance channel complexes, $Zr^+(CH_4)(Ar)$ and $Zr^+(CH_4)_2$. $Zr^+(CH_4)_3$ has a combination ranging from η^2 to almost η^3 and $Zr^+(CH_4)_4$ has all η^2 CH₄. The most red shifted and most intense peaks are due to the symmetric stretch of proximate C-H bonds in nearly η^2 methane ($\angle Zr-C-H = 130-140^\circ$). Slightly less red shifted and intense peaks are due to nearly η^3 methane ($\angle Zr-C-H = 160-170^\circ$). In addition, there is a peak near 3000 cm⁻¹ due to stretches of distal C-H bonds, which is intense for η^3 complexes and weak for η^2 coordination. This peak is observed for n=1-3, but drops greatly in intensity for n=4.

The n=1-2 complexes each also have a single peak at low wavenumber, 2567 and 2582 cm⁻¹, respectively, which is due to an exit channel complex with an agostic carbene group, (H₂)ZrCH₂⁺. In (H₂)ZrCH₂⁺(CH₄) the H–H stretch is observed at 3355 cm⁻¹. It drops to 3325 cm⁻¹ upon Ar tagging.

Dehydrogenation products are observed when Zr^+ sequentially reacts with three or four

 CH_4 molecules. The products formed come from loss of H_2 from n=3-4, $ZrC_3H_{10}^+$ and $ZrC_4H_{14}^+$, and loss of H and H_2+H from n=4, $ZrC_4H_{13}^+$ and $ZrC_4H_{15}^+$. The spectra of these products are compared to simulated spectra at several levels of theory. The lowest energy isomers are structures with methyl and methane groups and the lowest spin state is preferred. $ZrC_3H_{10}^+$ and $ZrC_4H_{13}^+$ have two and three methyl groups and a methane to form $Zr(CH_3)_2^+(CH_4)$ and $Zr(CH_3)_3^+(CH_4)$, respectively, with η^3 hydrogen coordination of methane. $ZrC_4H_{14}^+$ is most likely a combination of two isomers of $Zr(CH_3)_2^+(CH_4)_2$ with different methane binding orientations. The lowest energy isomer of $ZrC_4H_{15}^+$ is predicted to be $ZrCH_3^+(CH_4)_3$, however, the best match to experiment is a slightly higher in energy isomer, singlet $HZrCH_2^+(CH_4)_3$, which has an agostic carbene, one almost η^3 methane and two methanes between η^2 and η^3 .

Supporting Information Available

Full references 51 and 52; a mass spectrum of the ions; a diagram of the two valve fast-flow reactor source; potential energy surface calculations for $Zr^+ + CH_4$ at B3LYP and M11L; catalysis reaction table for B3LYP and M11L; BDE and E_{rel} of the entrance channel complexes and reaction products at the M11L/aug-cc-pVTZ level of theory; simulated and experimental spectra and geometry of $Zr^+(CH_4)_2$; IR spectra of the H_2 stretch peak of $[Zr,C2,H8]^+$; BDE and E_{rel} of the dehydrogenation products at the M11L/aug-cc-pVTZ level of theory; reaction product spectra and geometries at M11L for the most likely isomers; unscaled simulated spectra for $ZrC_4H_{14}^+$ at the B3LYP/aug-cc-pVTZ level of theory; thermodynamics of C-H activation reactions at B3LYP and M11L; and the energies, geometries, vibrational frequencies, and intensities of each complex at the B3LYP/aug-cc-pVTZ level of theory (Tables S6, S7, S8, S9, S10, and S11).

Acknowledgement

Financial support from the National Science Foundation under award no. CHE-1856490 is gratefully acknowledged. The authors are grateful for computational resources provided by the Massachusetts Green High-Performance Computing Center (MGHPCC).

References

- Crabtree, R. H. Alkane C-H Activation and Functionalization with Homogeneous Transition Metal Catalysts: A Century of Progress A New Millennium in Prospect. J. Chem. Society, Dalton Trans. 2001, 2437–2450.
- (2) Webb, J. R.; Bolaño, T.; Gunnoe, T. Catalytic Oxy-Functionalization of Methane and Other Hydrocarbons: Fundamental Advancements and New Strategies. *ChemSusChem* 2011, 4, 37–49.
- (3) Cavaliere, V. N.; Mindiola, D. J. Methane: A New Frontier in Organometallic Chemistry. *Chem. Sci.* **2012**, *3*, 3356–3365.
- (4) Irikura, K. K.; Beauchamp, J. L. Osmium Tetroxide and its Fragment Ions in the Gas Phase: Reactivity with Hydrocarbons and Small Molecules. J. Am. Chem. Soc. 1989, 111, 75–85.
- (5) Buckner, S. W.; MacMahon, T. J.; Byrd, G. D.; Freiser, B. S. Gas-Phase Reactions of Niobium⁺ and Tantalum⁺ with Alkanes and Alkenes. Carbon-Hydrogen Bond Activation and Ligand-Coupling Mechanisms. *Inorg. Chem.* 1989, 28, 3511–3518.
- (6) Irikura, K. K.; Beauchamp, J. L. Electronic Structure Considerations for Methane Activation by Third-Row Transition-Metal Ions. J. Phys. Chem. 1991, 95, 8344–8351.
- (7) Irikura, K. K.; Beauchamp, J. L. Methane Oligomerization in the Gas Phase by Third-Row Transition-Metal Ions. J. Am. Chem. Soc. 1991, 113, 2769–2770.
- (8) Armentrout, P. B. Electronic State-Specific Transition Metal Ion Chemistry. *Annu. Rev. Phys. Chem.* **1990**, *41*, 313–344.
- (9) Shayesteh, A.; Lavrov, V. V.; Koyanagi, G. K.; Bohme, D. K. Reactions of Atomic Cations with Methane: Gas Phase Room-Temperature Kinetics and Periodicities in Reactivity. J. Phys. Chem. A 2009, 113, 5602–5611.

- (10) Roithová, J.; Schröder, D. Selective Activation of Alkanes by Gas-Phase Metal Ions. *Chem. Rev.* **2010**, *110*, 1170–1211.
- (11) Schwarz, H., Chemistry with Methane: Concepts Rather than Recipes. Angew. Chem. Int. Ed. 2011, 50, 10096–10115.
- (12) Schwarz, H., How and Why Do Cluster Size, Charge State, and Ligands Affect the Course of Metal-Mediated Gas-Phase Activation of Methane? Isr. J. Chem. 2014, 54, 1413–1431.
- (13) Armentrout, P. B. Methane Activation by 5d Transition Metals: Energetics, Mechanisms, and Periodic Trends. *Chem.: Eur. J.* **2017**, *23*, 10–18.
- (14) Armentrout, P. B. Guided Ion Beam Studies of Transition Metal-ligand Thermochemistry. *Int. J. Mass Spectrom.* **2003**, *227*, 289–302.
- (15) Sievers, M.; Chen, Y.; Haynes, C.; Armentrout, P. Activation of CH₄, C₂H₆, and C₃H₈ by Gas-Phase Nb⁺ and the Thermochemistry of Nb-Ligand Complexes. *Int. J. Mass Spectrom.* **2000**, *196*, 149–170.
- (16) Ranasinghe, Y. A.; MacMahon, T. J.; Freiser, B. S. Formation of Thermodynamically Stable Dications in the Gas Phase by Thermal Ion-Molecule Reactions: Tantalum²⁺ and Zirconium²⁺ with Small Alkanes. *J. Phys. Chem.* **1991**, *95*, 7721–7726.
- (17) van Koppen, P. A. M.; Kemper, P. R.; Bushnell, J. E.; Bowers, M. T. Methane Dehydrogenation by Ti⁺: A Cluster-Assisted Mechanism for σ-Bond Activation. J. Am. Chem. Soc. 1995, 117, 2098–2099.
- (18) Armentrout, P. B.; Sievers, M. R. Activation of CH₄ by Gas-Phase Zr⁺ and the Thermochemistry of Zr-Ligand Complexes. *J. Phys. Chem. A* **2003**, *107*, 4396–4406.
- (19) Sievers, M. R.; Armentrout, P. B. Activation of C_2H_6 , C_3H_8 , and c- C_3H_6 by Gas-Phase

- Zr⁺ and the Thermochemistry of Zr-Ligand Complexes. *Organometallics* **2003**, *22*, 2599–2611.
- (20) Cummins, C. C.; Baxter, S. M.; Wolczanski, P. T. Methane and Benzene Activation via Transient (t-Bu₃SiNH)₂Zr=NSi-t-Bu₃. J. Am. Chem. Soc. **1988**, 110, 8731–8733.
- (21) Wolczanski, P. T. Activation of Carbon-Hydrogen Bonds via 1,2-RH-Addition/-Elimination to Early Transition Metal Imides. *Organometallics* **2018**, *37*, 505–516.
- (22) Fontaine, P. P.; Figueroa, R.; McCann, S. D.; Mort, D.; Klosin, J. Synthesis and Scale-up of Imino-Enamido Hafnium and Zirconium Olefin Polymerization Catalysts.

 Organometallics 2013, 32, 2963–2972.
- (23) Klosin, J.; Fontaine, P. P.; Figueroa, R. Development of Group IV Molecular Catalysts for High Temperature Ethylene-α-Olefin Copolymerization Reactions. Acc. Chem. Res. 2015, 48, 2004–2016.
- (24) Kamitani, M.; Pinter, B.; Chen, C.-H.; Pink, M.; Mindiola, D. J. Mononuclear and Terminal Zirconium and Hafnium Methylidenes. Angew. Chem. Int. Ed. 2014, 53, 10913–10915.
- (25) Lang, S. M.; Bernhardt, T. M. Gas Phase Metal Cluster Model Systems for Heterogeneous Catalysis. *Phys. Chem. Chem. Phys.* **2012**, *14*, 9255–9269.
- (26) Oomens, J.; Sartakov, B. G.; Meijer, G.; von Helden, G. Gas-phase Infrared Multiple Photon Dissociation Spectroscopy of Mass-selected Molecular Ions. *Int. J. Mass Spectrom.* **2006**, *254*, 1–19.
- (27) MacAleese, L.; Maître, P. Infrared Spectroscopy of Organometallic Ions in the Gas Phase: From Model to Real World Complexes. Mass Spectrom. Rev. 2007, 26, 583– 605.

- (28) Duncan, M. A. Infrared Spectroscopy to Probe Structure and Dynamics in Metal Ion-Molecule Complexes. *Int. Rev. Phys. Chem.* **2003**, *22*, 407–435.
- (29) Roithová, J. Characterization of Reaction Intermediates by Ion Spectroscopy. *Chem. Soc. Rev.* **2012**, *41*, 547–559.
- (30) Rodriguez, O.; Lisy, J. M. Infrared Spectroscopy of Li⁺(CH₄)_n, n=1-9, Clusters. *Chem. Phys. Lett.* **2011**, *502*, 145–149.
- (31) Poad, B.; Thompson, C.; Bieske, E. Infrared Spectra of Mass-Selected Al⁺-(CH₄)_n n=1-6 Clusters. *Chem. Phys.* **2008**, *346*, 176–181.
- (32) Dryza, V.; Bieske, E. J. Infrared Spectra and Density Functional Theory Calculations for Mn⁺-(CH₄)_n (n=1-6) Clusters. *Int. J. Mass Spectrom.* **2010**, *297*, 46–54.
- (33) Citir, M.; Altinay, G.; Austein-Miller, G.; Metz, R. B. Vibrational Spectroscopy and Theory of Fe⁺(CH₄)_n (n=1-4). *J. Phys. Chem. A* **2010**, *114*, 11322–11329.
- (34) Kocak, A.; Sallese, Z.; Johnston, M. D.; Metz, R. B. Vibrational Spectroscopy of $\mathrm{Co^+(CH_4)_n}$ and $\mathrm{Ni^+(CH_4)_n}$ (n=1-4). *J. Phys. Chem. A* **2014**, *118*, 3253–3265.
- (35) Kocak, A.; Ashraf, M. A.; Metz, R. B. Vibrational Spectroscopy Reveals Varying Structural Motifs in Cu⁺(CH₄)_n and Ag⁺(CH₄)_n (n=1-6). *J. Phys. Chem. A* **2015**, *119*, 9653–9665.
- (36) Gentleman, A. S.; Green, A. E.; Price, D. R.; Cunningham, E. M.; Iskra, A.; Mackenzie, S. R. Infrared Spectroscopy of Au⁺(CH₄)_n Complexes and Vibrationally-Enhanced C-H Activation Reactions. *Top. Catal.* 2018, 61, 81–91.
- (37) Cheng, Y. C.; Chen, J.; Ding, L. N.; Wong, T. H.; Kleiber, P. D.; Liu, D. K. Photodissociation Spectroscopy of MgCH₄⁺. J. Chem. Phys. **1996**, 104, 6452–6459.
- (38) Chen, J.; Cheng, Y. C.; Kleiber, P. D. Photodissociation Spectroscopy of CaCH₄⁺. J. Chem. Phys. **1997**, 106, 3884–3890.

- (39) Hayes, T.; Bellert, D.; Buthelezi, T.; Brucat, P. The Photodissociation of $V^+ \cdot CH_4$. Chem. Phys. Lett. **1997**, 264, 220–224.
- (40) Lu, W. Y.; Wong, T. H.; Kleiber, P. Photochemistry of Zn⁺(CH₄). *Chem. Phys. Lett.* **2001**, *347*, 183–188.
- (41) Lapoutre, V. J. F.; Redlich, B.; van der Meer, A. F. G.; Oomens, J.; Bakker, J. M.; Sweeney, A.; Mookherjee, A.; Armentrout, P. B. Structures of the Dehydrogenation Products of Methane Activation by 5d Transition Metal Cations. J. Phys. Chem. A 2013, 117, 4115–4126.
- (42) Simon, A.; Lemaire, J.; Boissel, P.; Maître, P. Competition Between Agostic WCH₂⁺ and HWCH⁺: A Joint Experimental and Theoretical Study. *J. Chem. Phys.* **2001**, 115, 2510–2518.
- (43) Perera, M.; Metz, R. B.; Kostko, O.; Ahmed, M. Vacuum Ultraviolet Photoionization Studies of PtCH₂ and H-Pt-CH₃: A Potential Energy Surface for the Pt⁺CH₄ Reaction. *Angew. Chem. Int. Ed.* **2013**, *52*, 888–891.
- (44) Wheeler, O. W.; Salem, M.; Gao, A.; Bakker, J. M.; Armentrout, P. B. Activation of C-H Bonds in Pt⁺ + xCH₄ Reactions, where x=1-4: Identification of the Platinum Dimethyl Cation. J. Phys. Chem. A **2016**, 120, 6216–6227.
- (45) Armentrout, P. B.; Stevenson, B. C.; Yang, F.; Wensink, F. J.; Lushchikova, O. V.; Bakker, J. M. Infrared Spectroscopy of Gold Carbene Cation (AuCH₂⁺): Covalent or Dative Bonding? J. Phys. Chem. A 2019, 123, 8932–8941.
- (46) Armentrout, P. B.; Kuijpers, S. E. J.; Lushchikova, O. V.; Hightower, R. L.; Boles, G. C.; Bakker, J. M. Spectroscopic Identification of the Carbyne Hydride Structure of the Dehydrogenation Product of Methane Activation by Osmium Cations. J. Am. Soc. Mass Spectrom. 2018, 29, 1781–1790.

- (47) Wheeler, O. W.; Salem, M.; Gao, A.; Bakker, J. M.; Armentrout, P. Sequential Activation of Methane by Ir⁺: An IRMPD and Theoretical Investigation. *Int. J. Mass Spectrom.* **2019**, *435*, 78–92.
- (48) Simon, A.; MacAleese, L.; Boissel, P.; Maître, P. Towards the Characterization of the Mechanism of the Sequential Activation of Four Methane Molecules by Ta⁺. *Int. J. Mass Spectrom.* **2002**, *219*, 457–473.
- (49) Husband, J.; Aguirre, F.; Ferguson, P.; Metz, R. B. Vibrationally Resolved Photofragment Spectroscopy of FeO⁺. J. Chem. Phys. **1999**, 111, 1433–1437.
- (50) Kocak, A.; Austein-Miller, G.; Pearson, W. L.; Altinay, G.; Metz, R. B. Dissociation Energy and Electronic and Vibrational Spectroscopy of Co⁺(H₂O) and Its Isotopomers. J. Phys. Chem. A 2013, 117, 1254–1264.
- (51) Gordon, I. E. et al. The HITRAN2016 Molecular Spectroscopic Database. *J. Quant. Spectrosc. Radiat. Transfer* **2017**, *203*, 3–69.
- (52) Frisch, M. J. et al. Gaussian Prevision D.01. 2013; Gaussian Inc. Wallingford CT.
- (53) Peverati, R.; Truhlar, D. G. M11-L: A Local Density Functional That Provides Improved Accuracy for Electronic Structure Calculations in Chemistry and Physics. J. Phys. Chem. Lett. 2012, 3, 117–124.
- (54) Sievers, M. R.; Chen, Y.-M.; Elkind, J. L.; Armentrout, P. B. Reactions of Y^+ , Zr^+ , Nb^+ , and Mo^+ with H_2 , HD, and D_2 . *J. Phys. Chem.* **1996**, *100*, 54–62.
- (55) Bushnell, J. E.; Kemper, P. R.; van Koppen, P.; Bowers, M. T. Mechanistic and Energetic Details of Adduct Formation and σ-bond Activation in Zr⁺(H₂)_n Clusters. J. Phys. Chem. A 2001, 105, 2216–2224.

- (56) Ruscic, B.; Bross, D. H. ATcT Thermochemical Values ver. 1.122 of the Thermochemical Network. 2019; https://atct.anl.gov/ThermochemicalData/version1. 122/index.php.
- (57) Yoshizawa, K.; Shiota, Y.; Yamabe, T. Intrinsic Reaction Coordinate Analysis of the Conversion of Methane to Methanol by an Iron-oxo Species: A Study of Crossing Seams of Potential Energy Surfaces. J. Chem. Phys. 1999, 111, 538–545.
- (58) Toth, R. A.; Brown, L. R.; Hunt, R. H.; Rothman, L. S. Line Parameters of Methane from 2385 to 3200 cm⁻¹. *Appl. Opt.* **1981**, *20*, 932–935.
- (59) Loh, Z. M.; Wilson, R. L.; Wild, D. A.; Bieske, E. J.; Lisy, J. M.; Njegic, B.; Gordon, M. S. Infrared Spectra and ab initio Calculations for the F⁻(CH₄)_n (n = 1-8) Anion Clusters. J. Phys. Chem. A **2006**, 110, 13736–13743.
- (60) Cho, H. G.; Wang, X.; Andrews, L. The C-H Activation of Methane by Laser-Ablated Zirconium Atoms: CH₂=ZrH₂, the Simplest Carbene Hydride Complex, Agostic Bonding, and (CH₃)₂ZrH₂. J. Am. Chem. Soc. **2005**, 127, 465–473.
- (61) Andrews, L.; Cho, H.-G.; Wang, X. [H₂C=ZrH₂]: The Simplest Carbene Hydride Complex, Agostic Bonding, and C-H Activation of CH₄ to Form [(CH₃)₂ZrH₂]. Angew. Chem. Int. Ed. 2005, 44, 113–116.
- (62) Roos, B. O.; Lindh, R.; Cho, H. G.; Andrews, L. Agostic Interaction in the Methylidene Metal Dihydride Complexes H₂MCH₂ (M = Y, Zr, Nb, Mo, Ru, Th, or U). J. Phys. Chem. A 2007, 111, 6420–6424.
- (63) van Koppen, P. A. M.; Perry, J. K.; Kemper, P. R.; Bushnell, J. E.; Bowers, M. T. Activation of Methane by Ti⁺: A Cluster Assisted Mechanism for σ-Bond Activation, Experiment, and Theory. Int. J. Mass Spectrom. 1999, 185-187, 989–1001.

Graphical TOC Entry

